Trust & Quality

Inspecta

INSPECTA

TECHNICAL REPORT

SKB

Analysis of PWR canister inserts using data acquired from PWR material

Report No.: 50010510-1

Revision No.: 8

INSPECTA TECHNOLOGY AB

BOX 30100 104 25 STOCKHOLM SWEDEN TEL (+46) 8 5011 3000 FAX (+46) 8 5011 3001 www.inspecta.com

Date	Our project No.
2014-01-31	50010510
Approved by	Organizational unit
Keivan Ashhami	Inspecta Technology AB
Customer	Customer reference
SKB AB	Magnus Johansson, Mikael Jonsson

Summary

SKB has asked Inspecta Technology AB to perform a damage tolerance analysis of the PWR iron insert both in the case of a pressure load and a shear load. The purpose of the analysis is to use material data for PWR inserts and compare the results with earlier calculations using material data for BWR inserts.

The main conclusions from the damage tolerance analysis are:

- The limit pressure load is higher using PWR insert material data. This shows that the results using BWR stress-strain data are conservative as regards to plastic collapse of the PWR canister. This is also true in the case of circular defects present in the PWR insert.
- In the case of a pressure load, the acceptable defect sizes are not influenced by the assumption regarding fracture toughness values. The results using BWR- or PWR-data are identical, since compressive stresses dominate when an external pressure is applied to the canister.
- In the case of a shear load, the acceptable defect sizes are slightly influenced by using PWR insert fracture toughness data together with the PWR insert stress-strain curve and the difference in geometry between the BWR and PWR canisters. The resulting acceptable defect depth for semi-elliptical surface defects are a_{acc} = 4.1 mm (for a PWR insert) and a_{acc} = 4.5 mm (for a BWR insert).

Report title	Subject Group
Analysis of PWR canister inserts using data acquired from PWR material	
	Index terms
	PWR, Canister inserts, Damage tolerance analysis
Work carried out by	Distribution
Peter Dillström, Tobias Bolinder, Etienne Bonnaud	☒ No distribution without permission from the customer or Inspecta Technology AB.
Work verified by	☐ Limited internal distribution in Inspecta Technology AB.
Lars Alverlind	☐ Unrestricted distribution.

Table of content *Page*

1 INTRODUCTION

Nuclear waste in Sweden is handled by the Swedish Nuclear Fuel and Waste Management Co, SKB. In the proposed final repository, copper canisters with a nodular cast iron insert containing spent nuclear fuel are surrounded by bentonite clay and deposited at approximately 400 m depth in saturated, granitic rock.

The canisters consist of a pressure-bearing insert of nodular cast iron with a steel lid, Fig. 1.1. The insert contains channels for the fuel assemblies, 12 in the BWR version and 4 in the PWR version. The insert is surrounded by an outer corrosion barrier of copper.

Figure 1.1. Canister for final depository of spent nuclear fuel.

In the repository the canisters will be loaded in compression by the hydrostatic pressure and the swelling pressure from the surrounding bentonite. The design pressure for the canisters has been set to be 45 MPa [1]. A damage tolerance analysis of both the BWR and the PWR insert, using pressure loads, has been presented in [2]. In the analysis presented in [2], no PWR insert material data were available and therefore only BWR insert data was used in the analysis.

The effect on the canister by a shear load has been investigated in [3]. A damage tolerance analysis of the BWR cast iron insert, using an earthquake induced rock shear load, has been presented in [4]. Although an analysis of the PWR insert was presented in [3] (using BWR insert data), no damage tolerance analysis for a PWR insert was conducted in [4].

SKB has presented material data for PWR inserts and it is now possible to do a damage tolerance analysis of PWR inserts using PWR data [5-10]. SKB has therefore asked Inspecta Technology AB to perform both revised and new damage tolerance analyses of the PWR cast iron insert. The purpose of this report is to provide a basis for assessing the quality requirements for PWR data. The report should not be considered to be a final design analysis report of the PWR insert, but should be viewed as an estimate using PWR data when the analysis were performed.

2 MATERIAL DATA

In order to perform a damage tolerance analysis of the PWR insert, using pressure loads, a new stress-strain curve in compression and initiation fracture toughness is needed [2]. This is given in Section 2.1 and 2.3. When performing a damage tolerance analysis of the PWR insert, using an earthquake induced rock shear load, a new stress-strain curve in tension and fracture toughness data including some stable crack growth is needed [4]. This is given in Section 2.2 and 2.3.

2.1 Stress-strain curve in compression

In the old damage tolerance analysis of the PWR insert, using pressure loads, a representative stress-strain curve was selected based on compressive testing of BWR inserts I24 and I25 [2]. This was considered to be a conservative approach for BWR inserts, since more recent data from manufactured BWR inserts have showed higher values [1].

In 2010, SKB performed compression testing of PWR inserts IP17 and IP19 [5]. 54 tests were performed and test number IP19M KP4 were chosen to be a representative stress-strain curve in the new damage tolerance analysis (since it was taken from the middle part of the insert where the lowest stress-strain material data could be found, see Fig. 2.1). A comparison between the old BWR insert data and the PWR insert data from IP19 can be found in Fig. 2.2. The data used in this analysis is also given in Table 2.1.

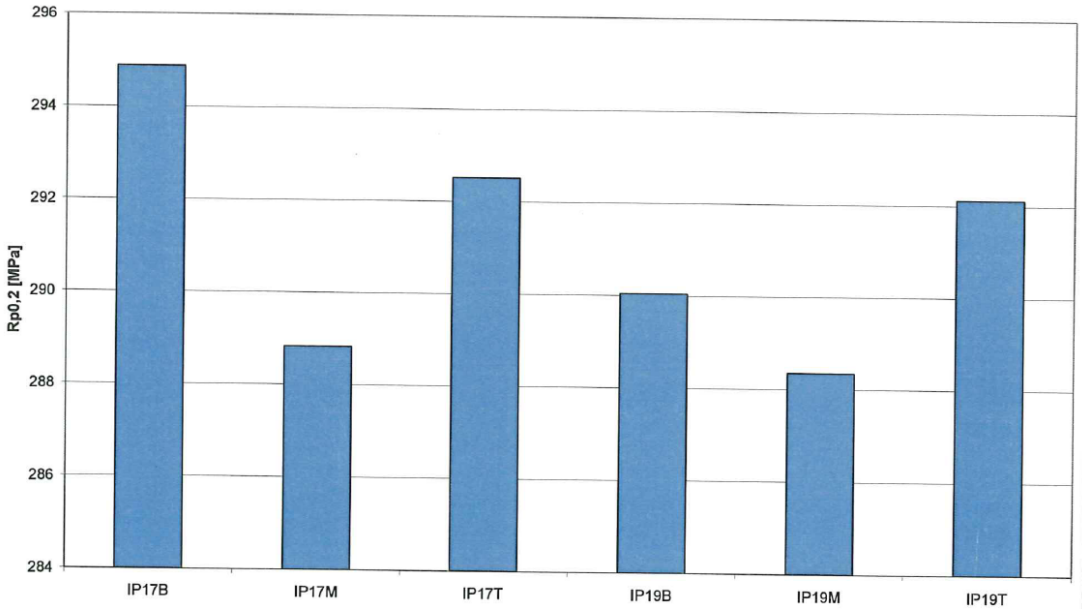

Figure 2.1. A comparison of the mean yield strength between the PWR inserts IP17 and IP19 using different parts of the inserts (B = bottom, M = middle, T = top) [5].

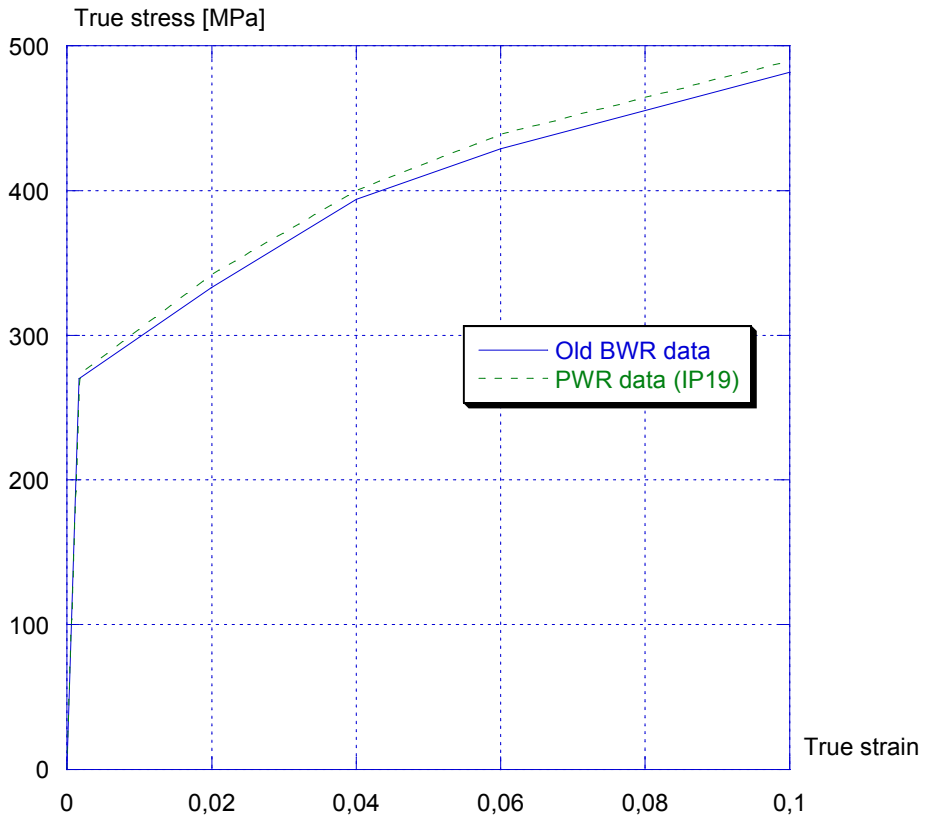

Figure 2.2. A comparison between different stress-strain curves in compression.

Table 2.1. Stress-strain curve in compression, using test number IP19M KP4.

True strain [-]	True stress [MPa]
0	0
0.0017786	273.51
0.02	342
0.04	400
0.06	439
0.10	490
0.12	508

As can be seen in Fig. 2.2, the old BWR insert data are lower than the PWR insert data from IP19. This indicates that the old damage tolerance analysis (as regards to plastic collapse) is conservative.

2.2 Stress-strain curve in tension

No damage tolerance analysis of the PWR insert, using an earthquake induced rock shear load, has previously been done. In order to perform such an analysis, SKB has done tension testing of PWR insert IP19 [6-8]. 21 tests were performed and test number IP19M-Prov1 was chosen to be a representative stress-strain curve in the new damage tolerance analysis (since it was taken from the middle part of the insert where the lowest stress-strain data could be found). A comparison between the old BWR insert data and the PWR insert data from IP19 can be found in Fig. 2.3. The data used in this analysis is also given in Table 2.2.

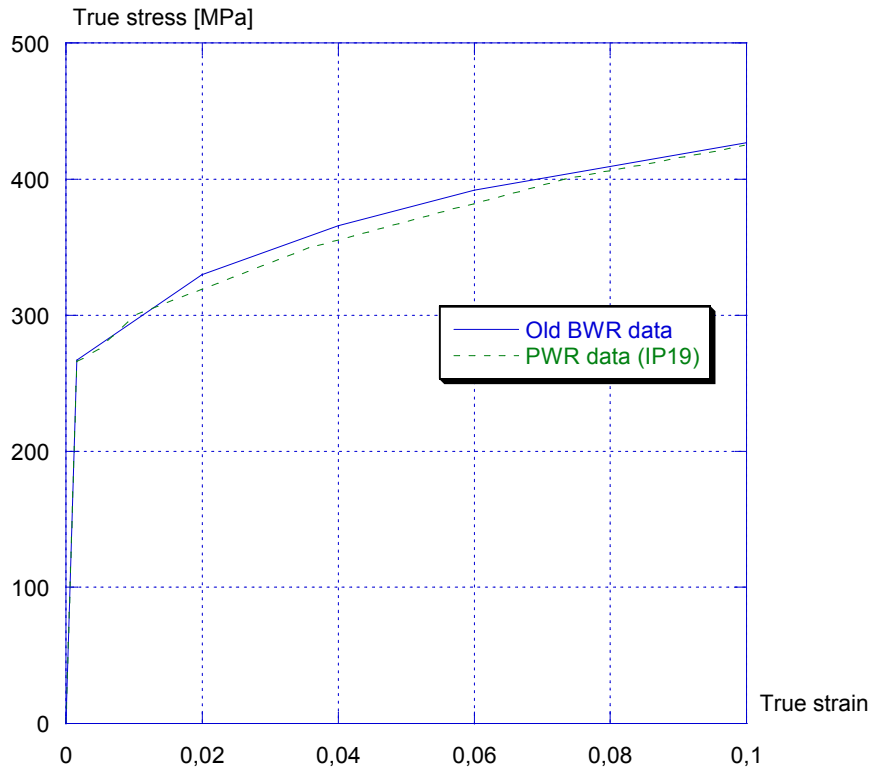

Figure 2.3. A comparison between different stress-strain curves in tension.

Table 2.2. Stress-strain curve in tension, using test number IP19M-Prov1.

True strain [-]	True stress [MPa]
0	0
0.001596	266
0.00477	275
0.0101	300
0.0359	350
0.0732	400
0.0996	425

As can be seen in Fig. 2.3, the old BWR insert data are higher than the PWR insert data from IP19. However, this difference is quite small up to a strain value of 1 %.

2.3 Fracture toughness data

In the damage tolerance analysis, defects are also postulated in the insert. Therefore, the fracture toughness for the nodular cast iron is needed to do a complete assessment. In the old damage tolerance analysis of the PWR insert, using pressure loads, initiation fracture toughness from BWR inserts was used in the analysis [2]. No damage tolerance analysis of the PWR insert, using an earthquake induced rock shear load, was conducted in [4].

In 2010, SKB performed fracture toughness testing of PWR insert IP19 [9-10]. The testing was performed at the temperature 0°C. It is observed from the fracture toughness experiments that the crack propagation in this material experiences *J*-dominant stable crack growth. Therefore, the fracture toughness data presented in Table 2.3 has data both for initiation and including 2 mm of stable crack growth. Only qualified data, according to ASTM E1820 (Standard Test Method for Measurement of Fracture Toughness), are given in Table 2.3.

Table 2.3. Fracture toughness data, at 0°C, for the PWR insert IP19 [9-10].

Fracture toughness	Data
J_{Ic} [kN/m], at initiation	24, 33, 26, 36, 32, 39
J_{2mm} [kN/m], at 2 mm stable crack growth	76.4, 75.6, 84.5, 90.6, 87.0, 101.7

Using the fracture toughness data given in Table 2.3, we can calculate the sample mean value and the sample standard deviation using the equations below. The sample mean value is given as (n = number of samples):

$$m = \frac{1}{n}\sum_{i=1}^{n} x_i \ . \tag{2.1}$$

The unbiased sample standard deviation (the square root of the unbiased sample variance) is given as:

$$s = \sqrt{\frac{1}{n-1}\left[\sum_{i=1}^{n} x_i^2 - \frac{1}{n}\left(\sum_{i=1}^{n} x_i\right)^2\right]} \ . \tag{2.2}$$

From a sample we now have obtained single-valued estimates of the mean and standard deviation of the fracture toughness. These single-valued estimates represent our best estimate of the population values. In a damage tolerance analysis we want to use an estimate with a given confidence (i.e. 90%). Thus we are interested in the accuracy of these sample estimates. Confidence intervals represent a means of providing a range of values in which the true value can be expected to lie. In this investigation we will use approximate confidence intervals, using properties of the so-called Student's *t*-distribution and the χ^2-distribution [11].

Confidence interval for the population mean μ, when the population standard deviation σ is unknown, has the following form:

$$m - t_{\alpha/2,n-1}\left(\frac{s}{\sqrt{n}}\right) \le \mu \le m + t_{\alpha/2,n-1}\left(\frac{s}{\sqrt{n}}\right), \tag{2.3}$$

where $t_{\alpha/2,n-1}$ is the Student's *t*-distribution (using a two-sided interval) with a level of significance α and with $n-1$ degrees of freedom.

The confidence intervals given above now provide an interval in which we are $100(1-\alpha)$ percent confident that the population values lies within that given interval. Using the data from [9-10] we now can calculate estimates and confidence intervals for different fracture toughness distributions (J_{Ic} or J_{2mm}). These calculations are summarized in Table 2.4.

Table 2.4. Evaluated fracture toughness data for PWR insert IP19. Estimates of the population mean (using α = 0,1, i.e. 90% confidence).

Case	Sample mean *m*	Population mean μ
J_{Ic} [kN/m]	31.7	$26.9 \le \mu \le 36.4$
J_{2mm} [kN/m]	86.0	$78.0 \le \mu \le 94.0$

Conservative fracture toughness data, to be used in a damage tolerance analysis (with 90% confidence), is therefore $J_{Ic} = 27$ kN/m or $J_{2mm} = 78$ kN/m.

The initiation fracture toughness may also be expressed as K_{Jc} with a mean value equal to 76.4 MPa$\sqrt{\text{m}}$ and a fracture toughness value (with 90% confidence) equal to $K_{Jc} = 70.6$ MPa$\sqrt{\text{m}}$.

3 ANALYSIS OF PWR CANISTER INSERTS IN THE CASE OF A GLACIAL PRESSURE LOAD

In a damage tolerance analysis of the PWR insert, using pressure loads, two different failure modes are considered. These are plastic collapse (using a limit load analysis) and initiation of crack growth. Different failure criteria and safety margins are used in the two cases.

3.1 Limit load – Failure criteria and safety margins

In analysis of components used in the Swedish nuclear industry, acceptance criteria's are usually adopted from the American ASME code. In this report the criteria for limit load described in NB-3228.3 [12] is used. The purpose with the method described in NB-3228.3 is to show that the applied load do not go beyond 2/3 of calculated collapse load. If this can be shown, the limits of General Membrane Stress Intensity (NB-3221.1 [12]), Local Membrane Stress Intensity (NB-3221.2 [12]), and Primary Membrane Plus Primary Bending Stress Intensity (NB-3221.3 [12]) need not be satisfied at a specific location. The calculated collapse load is defined in NB-3213.25. In Fig. 3.1, obtained from 2004 ASME VIII Div 2 Appendix 6 article 6-153, it is graphically shown how the collapse load is defined. The angle θ is defined in the linear elastic part of the load-deformation curve. The *Collapse limit line* is defined by the angle φ = atan(2tan(θ)). The *Collapse load point* is defined as the point where the *Collapse limit line* crosses the calculated load-displacement curve.

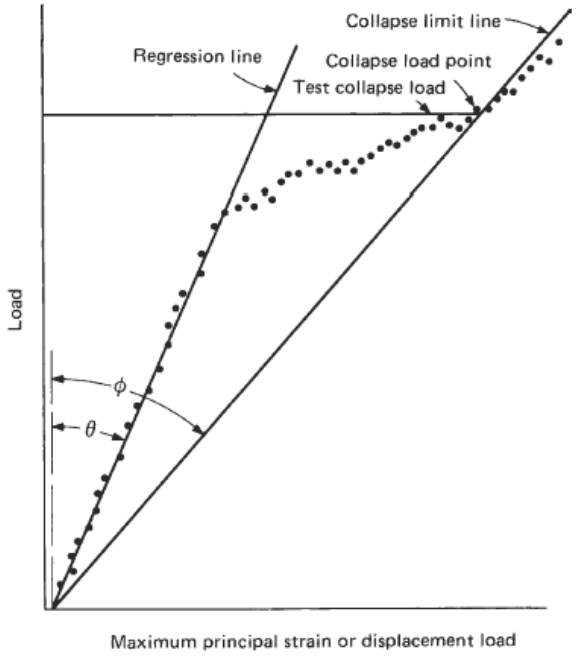

Figure 3.1. Definition of the collapse load.

3.2 Initiation of crack growth – Failure criteria and safety margins

In the damage tolerance analysis, with postulated defects, the critical defect size is given using the failure criteria $J = J_{mat}$ (or $K_{\mathrm{I}} = K_{mat}$) and the acceptable defect size is given using the criteria $J = J_{mat} / SF_J$ (or $K_{\mathrm{I}} = K_{mat} / SF_K$). In these equations, J is the applied J-value, J_{mat} is the fracture toughness (with or without some stable crack growth) of the nodular cast iron used in the insert. SF_J (or SF_K) is the safety factor used when calculating the acceptable defect size.

For the choice of safety factor SF_J, the objective has been to retain the safety margins expressed in ASME Sect. XI [13]. This means that SF_J = 10 (or SF_K = 3.16) is used in the case of normal operation or with loads that occur quite frequently. SF_J = 2 (or SF_K = 1.41) is then used for loads with a very low probability of occurrence. According to the design premises for the canister [1], the load case considered in this case (a glacial pressure load) is a normal load case. Therefore, SF_J should be equal to 10 in this case (or SF_K = 3.16).

3.3 Limit load – Damage tolerance analysis

A damage tolerance analysis of the PWR insert, using pressure loads, has already been presented in [2]. As mentioned earlier, a problem with that analysis was that no PWR insert material data were available and therefore only BWR insert data were used in the analysis. The purpose of the damage tolerance analysis in this section is therefore to do a new analysis, using the same assumptions as in [2], but with the PWR insert material data presented in section 2.

A complete parametric 2D model of the PWR canister, with the possibility to insert circular defects at arbitrary positions, was created using the ANSYS FE program [14] (see Fig. 3.2). To model the canister, the 8-noded element PLANE183 was used (in plane strain). Contact conditions were given between the copper shell and the insert and also between the insert and the channel tubes (using the contact element CONTA172 and TARGE169). More details on the modelling can be found in [2].

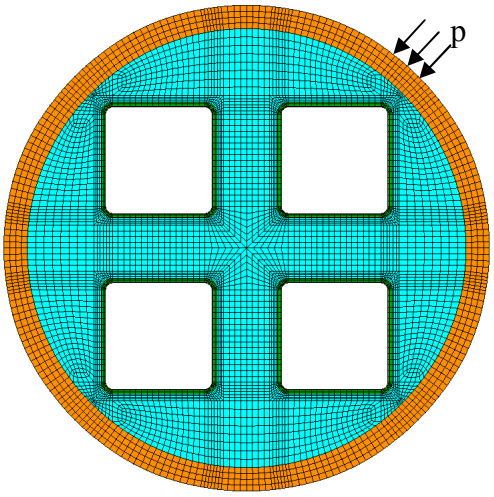

Figure 3.2. Element mesh of the PWR canister.

To check the influence of defects on the limit load, a circular defect was introduced in the insert. The defect position 7 according to [2] was chosen (i.e. position 7 in Fig. 3.3). The defect radius was given as 40 mm [2]. In the analyses a 2D-idealization of the canister has been used, which means that the postulated cavity defects are cylindrical with a height corresponding to the full length of the canister. This is a very conservative assumption.

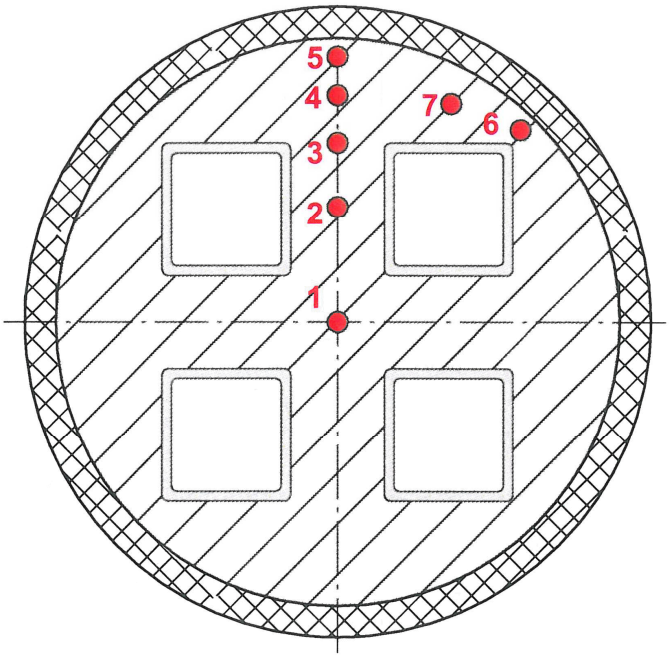

Figure 3.3. Postulated circular defect in position 7.

Boundary conditions were applied to the canister to prevent rigid body motion. The load was then applied as a uniform pressure on the entire outer surface of the canister. Limit load analyses were performed for a case without a defect and a case with a circular defect in position 7. The limit load analyses were conducted by means of step wise increasing the applied pressure load. In this way the load on the canister was increased for every step. To obtain the load deformation curve, the largest deformation was plotted against the corresponding load. Collapse load was calculated from the load-deformation curve as described in section 3.1.

In Table 3.1, the collapse loads are presented for the 2D models with a defect at position 7 and for the model without defects. The results from [2] using BWR insert material data, are also given in Table 3.1.

Table 3.1. Results from limit load analysis of the PWR insert with and without a circular defect.

	Without defect	With a circular defect in position 7
Using old BWR data [2]	127.4 MPa	71.3 MPa
Using PWR data from IP19	130.1 MPa	73.4 MPa

As given in Table 3.1, the limit load using PWR insert material data is higher than in the old analysis using BWR insert material data [2]. This shows that the results presented in [2] are conservative as regards to plastic collapse of the PWR canister.

3.4 Initiation of crack growth – Damage tolerance analysis

The allowable defect size for postulated defects, in various locations in the insert, was examined by a damage tolerance analysis that was reported in [2]. That analysis was made by calculating the stress intensity factor K_I in various locations and then compared, using a safety factor of $SF_K = 3.16$, to an initiation fracture toughness value (K_{Ic}) at a temperature 0°C. As mentioned earlier, a problem with that analysis was that no PWR insert fracture toughness data were available and therefore only BWR data were used in the analysis. The purpose of the damage tolerance analysis in this section is therefore to do a new analysis, using the same assumptions as in [2], but with the PWR insert material data presented in section 2.

Using the 2D model given in section 3.3, stresses were calculated in the insert (the loading was a uniform pressure equal to 45 MPa). Semi-elliptical surface defects (with a defect length over depth ratio equal to six) were then postulated to exist in different locations (see Fig. 3.4). The software ProSACC [15] was then used, to get allowable defect sizes at these locations.

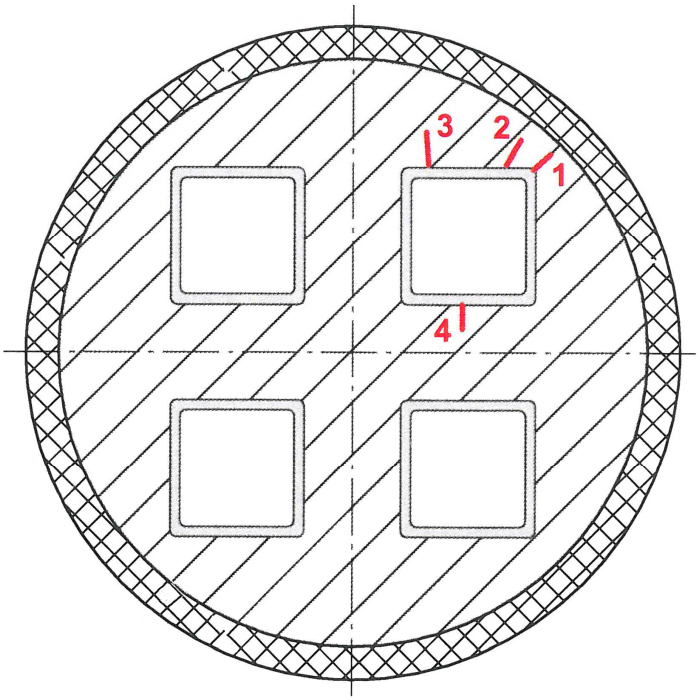

Figure 3.4. Locations of the postulated defects in PWR inserts.

The fracture toughness value used in the analysis was equal to $K_{Jc} = 70.6\ \text{MPa}\sqrt{\text{m}}$ (with 90% confidence). This should be compared to $K_{Jc} = 79.4\ \text{MPa}\sqrt{\text{m}}$, that was used in [2] given the data from BWR inserts. The calculated acceptable defect sizes are given in Table 3.2.

Table 3.2. Acceptable defect sizes for postulated semi-elliptical surface cracks.

Defect location	l_{acc} [mm]	a_{acc} [mm]
1	> 189.1	> 31.5
2	> 319.3	> 53.2
3	> 672.9	> 112.2
4	> 624.0	> 104.0

The results presented in Table 3.2 are identical to the results presented in [2] using higher fracture toughness values. These results are actually almost independent of the given fracture toughness value, since compressive stresses dominates in the case of an external pressure equal to 45 MPa. The maximum defect size, a, that can be analysed corresponds to 80% of the wall thickness. This limitation originates from the range of applicability of the applied computer model (postulated surface cracks can be analysed up to 80% of the wall thickness).

4 ANALYSIS OF PWR CANISTER INSERTS IN THE CASE OF A ROCK SHEAR LOAD

The analyses of the PWR canister are conducted with the FE program ABAQUS [16]. A submodelling technique is used to introduce different defects in the PWR canister. When using a submodelling technique, a global model is used to retain the stresses and displacements of the canister. From these global results, the areas of interest are identified. In these areas the submodels containing the defects are introduced. The deformations from the global model are applied at the boundary of the submodel. From the submodel the *J*-integral results are then obtained. In the analyses four different kinds of defects with different crack depths are introduced using a submodelling technique. The defects are introduced in three different areas see Fig. 4.1. In position 1 the surface defect are introduced, in position 2 internal defects with 2a= 1 mm, 5 mm, 10 mm are introduced and in position 3 all the internal defects are introduced. A total of 43 submodels are analyzed. Below is a summary of the examined cases.

Global models (only the dominating case with a bentonite density 2050 kg/m^3 was analyzed):

- Model6g_PWR2_normal_quarter_2050ca3 (Bentonite density 2050 kg/m^3).

Submodels:

- Semi-elliptical surface crack with a crack depth a = 1 mm, 5 mm, 10 mm and a crack length $2c = 6a$ = 6 mm, 30 mm, 60 mm.
- Semi-circular surface crack with a crack depth a = 1 mm, 5 mm, 10 mm and a crack length $2c = 2a$ = 2 mm, 10 mm, 20 mm.
- Elliptical internal crack with a crack depth $2a$ = 1 mm, 5 mm, 10 mm and a crack length $2c = 12a$ = 6 mm, 30 mm, 60 mm.
- Circular internal crack with a crack depth $2a$ = 1 mm, 5 mm, 10 mm, 20 mm and a crack length $2c = 2a$ = 1 mm, 5 mm, 10 mm, 20 mm.

The crack depth parameter a and the crack length parameter c is defined in Fig. 4.6 (surface cracks) and Fig. 4.11 (internal cracks).

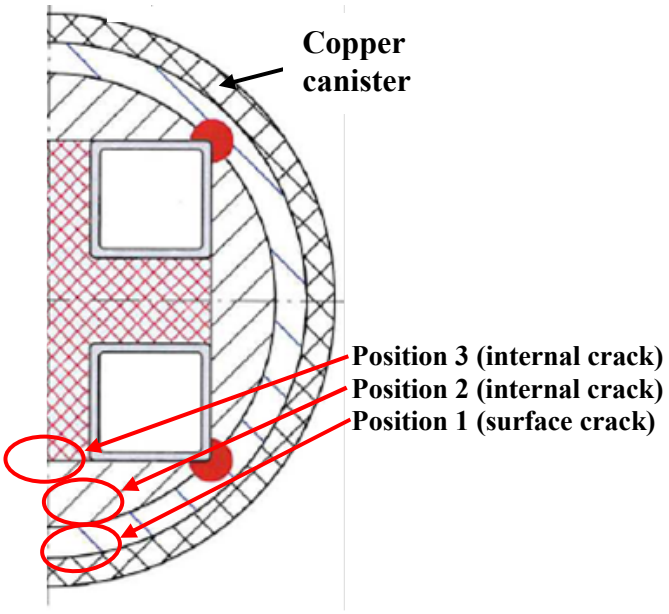

Figure 4.1. Positioning of submodels (as defined in sect. 4.2.1-4.2.2).

4.1 Global FE-model

The global FE-model obtained from Hernelind [3] is made up by 8 node brick elements (C3D8) and 8 node brick elements with reduced integration (C3D8R). Contact is defined between the copper shell and the nodular cast iron insert. The channel tubes are modelled as welded to the insert and therefore contribute as added material to the insert (this will probably overestimate the insert stresses and strains in this region). Only half the canister is modelled by using symmetry. In Fig. 4.2 the element mesh of the canister can be seen.

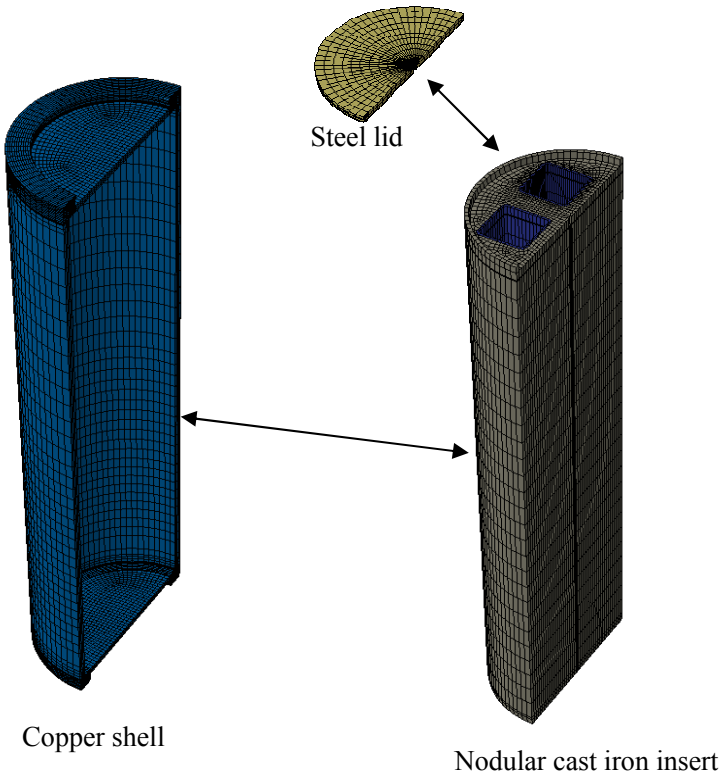

Figure 4.2. Global model of the PWR canister.

4.1.1 Boundary conditions, loading and material

Boundary conditions are defined as symmetry at the symmetry plane. Loads are applied as displacement history at the outer boundary of the copper canister. These displacements are obtained from Hernelind [3]. The loading history corresponds to the shear of the PWR canister including the bentonite clay. Three different load steps are applied corresponding to 0, 5 and 10 cm of shear (in the first step there exist initial stresses corresponding to the swelling pressure in the bentonite [3]). Boundary conditions and loads are shown in Fig. 4.3.

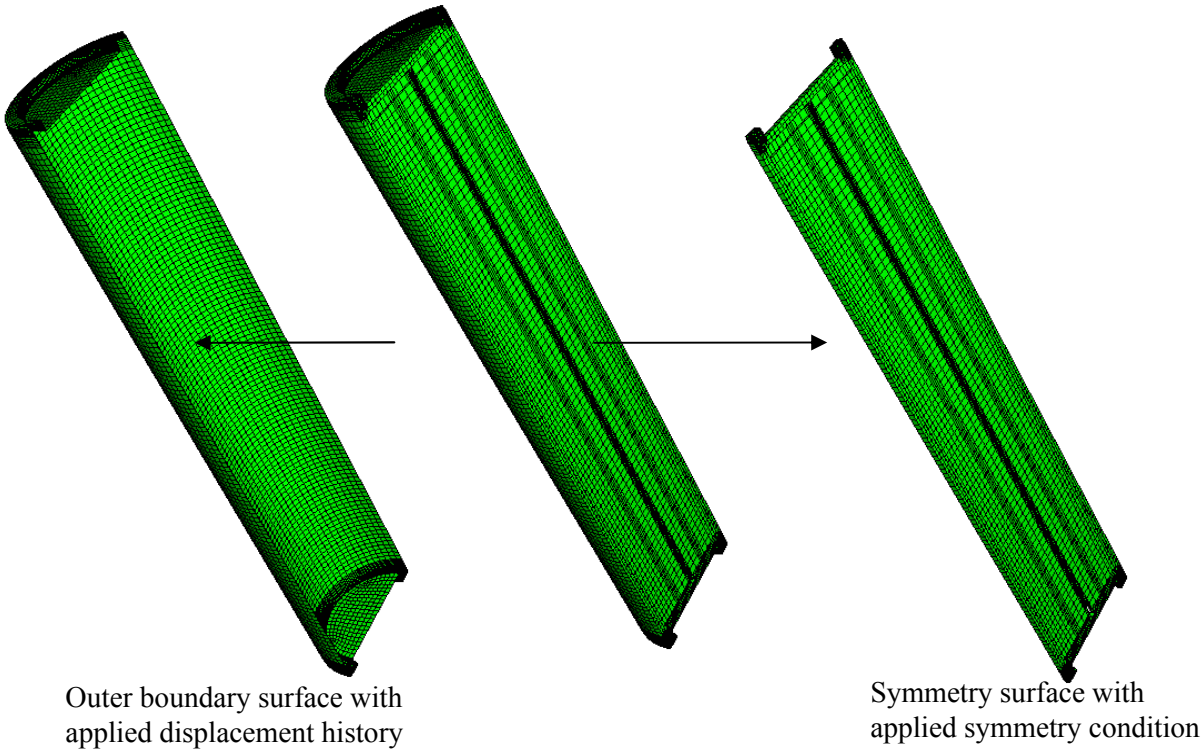

Figure 4.3. Applied boundary condition and displacement loading.

The materials are defined as elastic-plastic with isotropic hardening. The material data is taken from the damage tolerance analysis of BWR canister inserts [3-4], except the data for the PWR cast iron insert. The copper used for the copper shell is modelled with E = 120 GPa, ν = 0.308 and σ_y = 72 MPa. The nodular cast iron making up the iron insert is modelled according to section 2. with E = 166.7 GPa, ν = 0.32 and σ_y = 266 MPa. The steel making up the channel tubes is modelled with E = 210 GPa, ν = 0.30 and σ_y = 412 MPa. Stress-strain curves are given in Fig. 4.4 (using tension tests at room temperature and a normal strain rates). More information on the material models is given in [3]. Large-displacement formulation is used in all analyses.

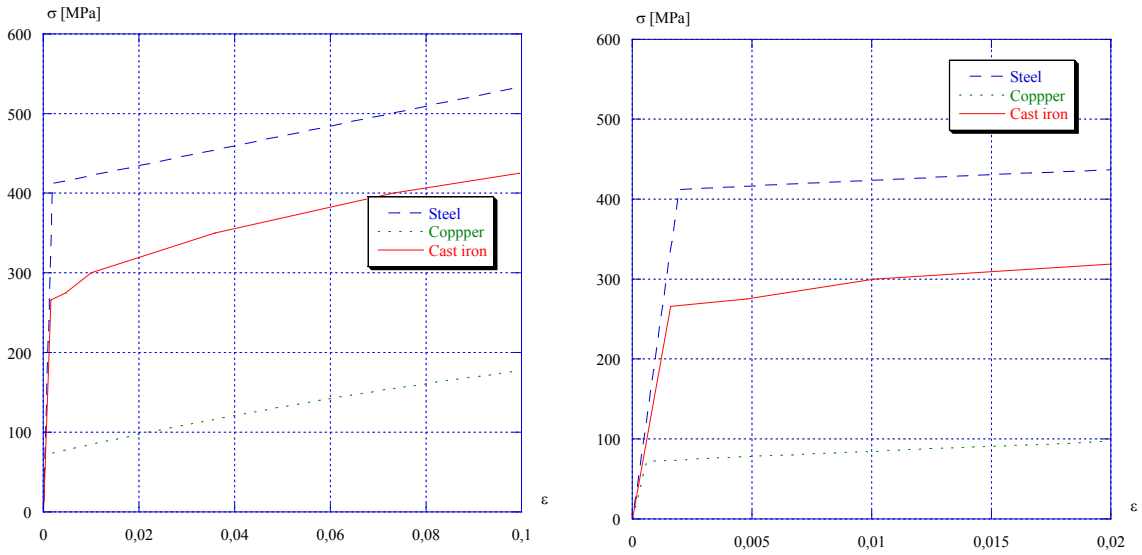

Figure 4.4. True stress – strain curves for copper, steel and nodular cast iron used in the analyses.

4.1.2 Results for the global models

The results obtained from the global models in this report are compared with the results obtained by Hernelind [3]. The comparison in Table 4.1 show very small differences. However, the differences can be explained by that the results are dependent on the loading history. The time increment with which the displacement history is applied is not that refined that it gives exactly the same results as those obtained by Hernelind [3]. The differences are considered to be small and not to influence the results significantly.

Table 4.1. Comparison for model6g_PWR2_normal_quarter_2050ca3.

Comparison between Hernelind and Inspectas global model without bentonite clay		
	Iron insert	
	Von Mises stress [MPa]	
	5 cm	10 cm
Hernelind	296.8	325.1
Inspecta	295.4	324.9
Difference [%]	0.5	-
	Steel tubes	
	Von Mises stress [MPa]	
	5 cm	10 cm
Hernelind	416.5	426.7
Inspecta	416.6	426.8
Difference [%]	-	-

The results from the global model are investigated to decide where to introduce the defect. The location where the max principal stress is the highest is identified, see Fig. 4.5. This governs at which height in the canister the submodels containing the defects are introduced (see section 4.2).

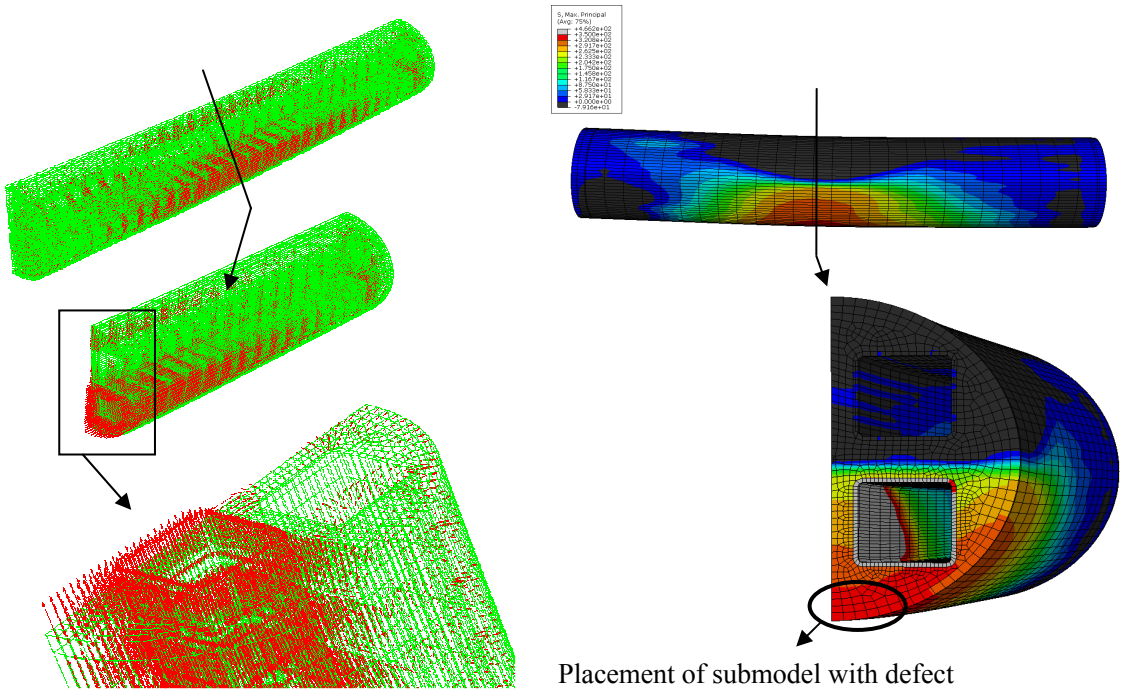

Figure 4.5. Identified location for submodels containing the defects.

4.2 Submodels at the location with max principal stress

Four different defects are modelled, three with three different crack depths and one with four different crack depths. For the submodells used at position 3 (see Fig. 4.1) only half the defect is modelled by using symmetry. This gives a total of 19 submodels. All submodels are made up by 20 node brick elements with reduced integration (C3D20R). To check this choice, a comparison was made using the elements C3D20, C3D20R (using reduced integration) and C3D20H (using a hybrid displacement/pressure formulation interpolation scheme). The difference, when comparing the calculated *J*-values, is quite small. In some cases the C3D20R elements introduced problems at the crack tip front. In these cases the C3D20 elements were used instead. All submodels use the same material models as their respective global model, see Fig. 4.4. Below the modelling of the different defects are described. Large-displacement formulation is used in all analyses.

4.2.1 FE-models of surface defects

Since the submodels containing surface defects are placed at the outer boundary of the nodular cast iron insert, part of the copper canister is also modelled for the submodel. This is done not to neglect any influence from the contact between the copper and iron surfaces. All six submodels are created as two rectangular blocks, one for the copper canister and one for the nodular cast iron casing. The submodels are created with the same external size, independent of defect and crack depth. The geometry of the models are shown in Fig. 4.6 with H = 100 mm, w = 120 mm, t_{copper} = 20 mm, t_{iron} = 30 mm a = 1, 5, 10 mm, for semi-elliptical defect $2c = 6a$ and for semi-circular defect $a = c$. One extra model without a defect is also created to check the accuracy of the submodelling technique. The models are also curved to match the radius of the canister.

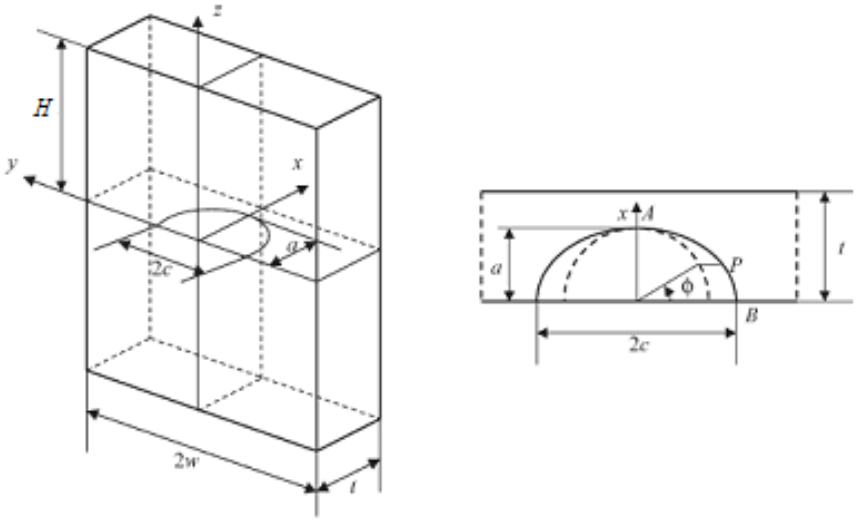

Figure 4.6. Geometry of a semi-elliptical surface defect.

The element mesh is focused towards the crack tip. The crack tip is modelled with a small notch as can be seen in Fig. 4.7.

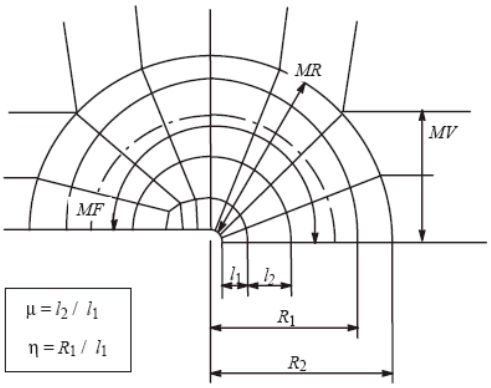

Figure 4.7. Focused element mesh towards the crack tip (*MF*, *MR*, and *MV* represents the number of elements in each direction according to the figure).

To decide the mesh refinement of the crack tip area, a quarter model of the surface crack is created. For the quarter model the variables R_1, R_2, η, μ and *MR* are held constant while *MF* and the number of elements along the crack front, *NA*, are varied (variable definition, see Fig. 4.7). From these analyses the *J*-integral is computed and compared. In Fig. 4.8 the results of this sensitivity analyses are shown. From the sensitivity analyses a crack tip mesh with *MF*=6, *MR*=10, *MV*=2 and 20 elements along the crack front are used in the analysis (since a sufficient number of elements along the crack front is needed).

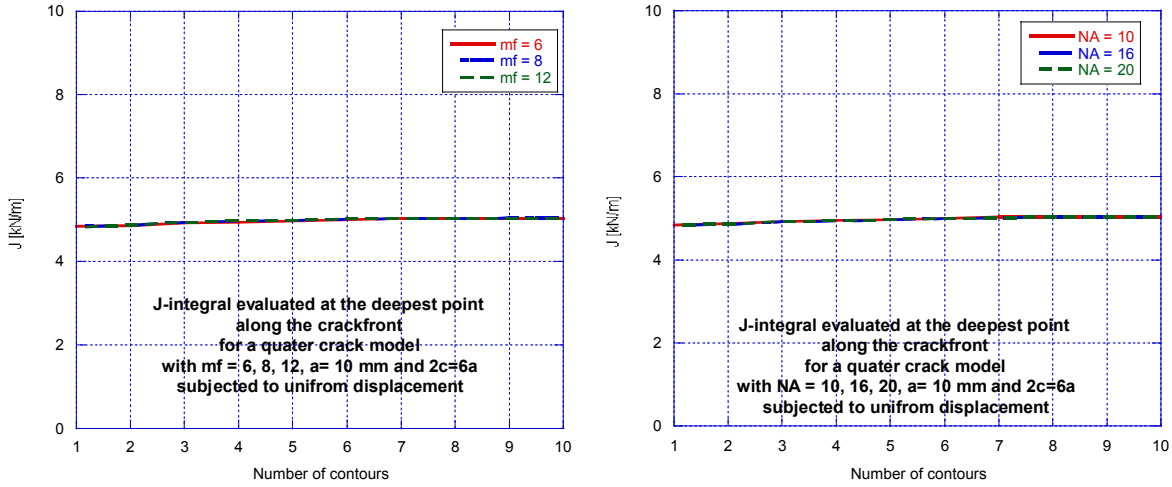

Figure 4.8. Results from the sensitivity analyses.

Below, in Fig. 4.9, a typical element mesh of the submodel containing a surface defect is shown.

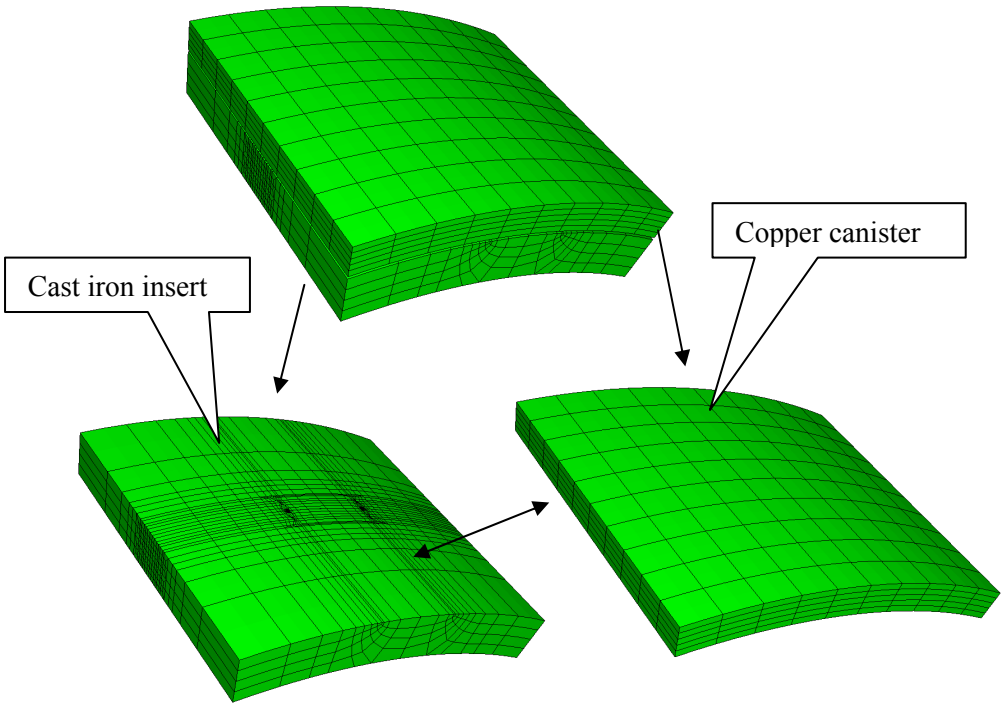

Figure 4.9. Element mesh for a submodel containing a surface defect with a = 10 mm.

Boundary conditions and loading for the submodel consist of displacements on the boundary obtained from the global model. These are automatically transferred from the global model to the boundary of the submodel and hence it is very important that the placement of the submodel relative the global model is correct. To check the correctness of the transferred displacements from the global model to the submodel a model without a crack is used. The stresses through the thickness are compared with the corresponding stresses in the global model. The results showed a good agreement between the global model and submodel as shown in Fig. 4.10.

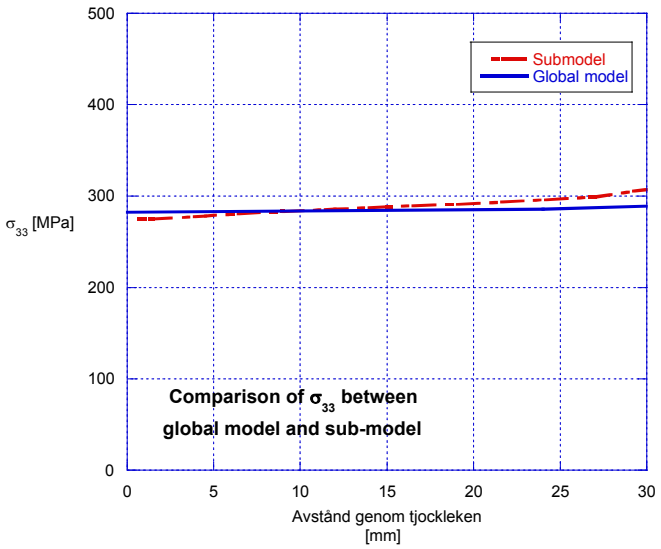

Figure 4.10. Stresses through the thickness for the submodel and the global model (stresses in the axial direction at a location with high axial stresses).

4.2.2 FE-models of internal defects

The submodels containing the elliptical and circular internal defects are created as rectangular blocks containing the defect. For the submodels used at position 3, symmetry is used to only model half the defect. In position 2 the maximum size of the submodel is limited by the smallest thickness between the outer boundary and the channels in the nodular cast iron insert. The chosen sizes used for the different defects at position 2 were based on a size sensitivity analysis. In position 3 the maximum size of the submodel is limited by the distance between symmetry boundary of the nodular cast iron insert and the channels. The geometry for the submodel is shown in Fig. 4.11. Seven different geometries are used for the different submodels as listed below. The elliptical defect is modelled with $2c = 12a$ and the circular with $2c = 2a$.

- $2a$ = 1 mm:
  Position 2: H = 30 mm, w = 30 mm and t = 30 mm
  Position 3: H = 20 mm, w = 25 mm and t = 50 mm (half model using symmetry)
- $2a$ = 5 mm:
  Position 2: H = 45 mm, w = 45 mm and t = 40 mm
  Position 3: H = 60 mm, w = 50 mm and t = 80 mm (half model using symmetry)
- $2a$ = 10 mm:
  Position 2: H = 60 mm, w = 60 mm and t = 45 mm
  Position 3: H = 60 mm, w = 50 mm and t = 100 mm (half model using symmetry)
- $2a$ = 20 mm:
  Position 3: H = 60 mm, w = 50 mm and t = 100 mm (half model using symmetry)

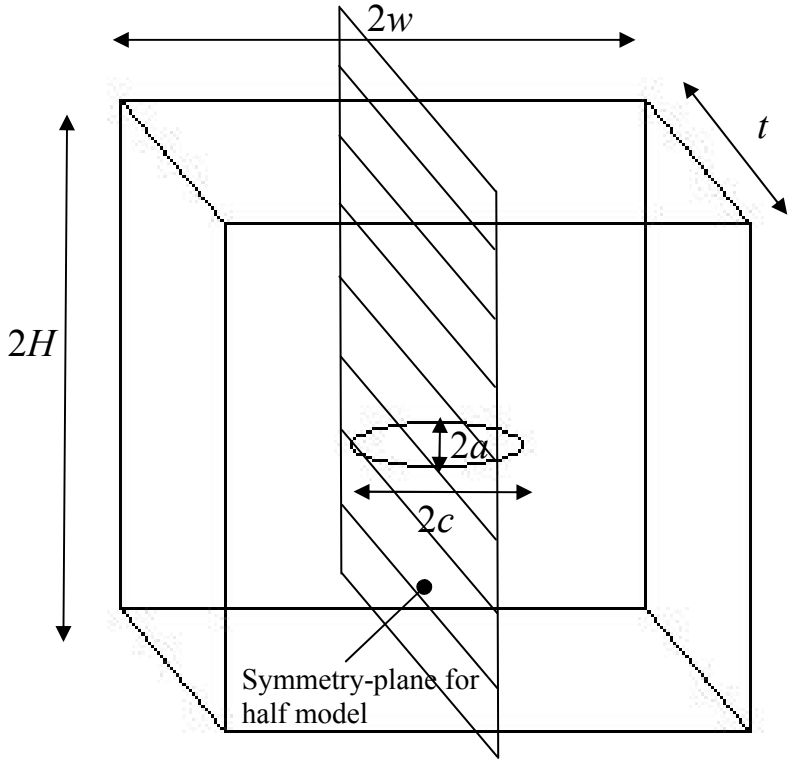

Figure 4.11. Geometry of the internal defect.

The element mesh is focused towards the crack tip. The crack tip is modelled with a small notch as can be seen in Fig. 4.7. The same mesh setup as for the surface defect is used for the internal defects at position 2 with the exception of number of elements along the crack front. For the internal defects the number of elements along the crack front is doubled to 40. For the internal defects at position 3 a crack tip mesh with *MF*=10, *MR*=8, *MV*=4 (defined in Fig. 4.7) and 20 elements along the crack front is used (half model using symmetry leads to half the number of elements along the crack front). In Fig. 4.12 the element mesh for a typical internal elliptical defect is shown.

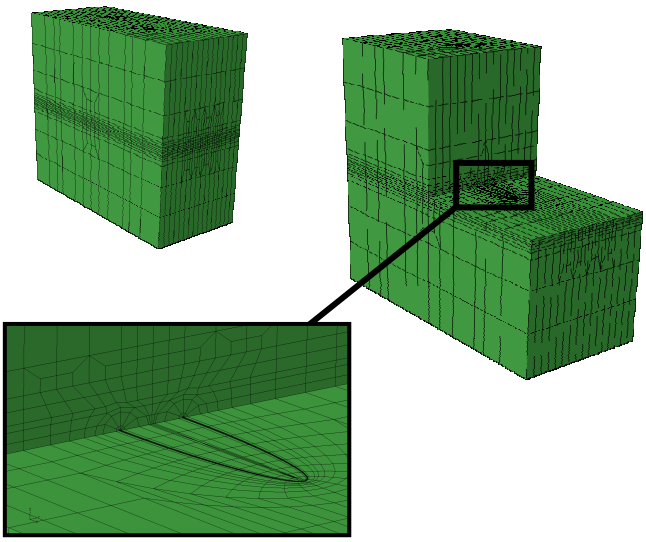

Figure 4.12. Element mesh for an elliptical internal defect.

Boundary conditions and loading for the submodel consist of displacements on the boundary obtained from the global model. These are automatically transferred from the global model to the boundary of the submodel. Additionally for the submodels in position 3 a symmetry boundary condition was applied at the symmetry plane of the submodel see Fig 4.13.

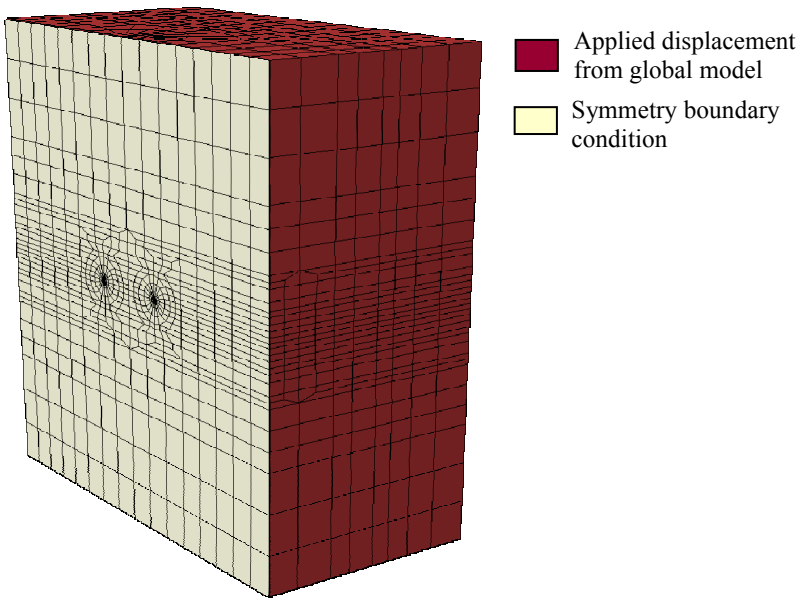

Figure 4.13. Boundary condition for sub models at position 3.

4.2.3 Results at the location with max principal stress

The results presented below, and in appendix A, are obtained using the different submodels. ABAQUS domain integral method is used to calculate the *J*-integral [16]. The results are given for *model6g_PWR2_normal_quarter_2050ca3* in Appendix A. The results show that the elliptical surface defects give much higher *J*-values than the circular surface defects. The internal defects do not give as high *J*-values as the surface defects. These trends between the different types of defects do correspond to handbook solutions for simpler geometries and loading conditions. It can also be seen that results from position 3 give slightly lower *J*-values compared with the same defects at position 2. The maximum *J*-value for the different submodels is summarized in Table 4.2-4.4.

Table 4.2. Maximum *J*-value [kN/m], along the crack front at position 1.

Defect	a = 1 mm Shear = 5-10 cm		a = 5 mm Shear = 5-10 cm		a = 10 mm Shear = 5-10 cm	
Semi-elliptical surface defect	8.97	21.89	47.76	122.5	79.97	206.6
Semi-circular surface defect	5.56	14.45	27.36	71.27	50.51	131.8

Table 4.3. Maximum *J*-value [kN/m], along the crack front at position 2.

Defect	$2a$ = 1 mm Shear = 5-10 cm		$2a$ = 5 mm Shear = 5-10 cm		$2a$ = 10 mm Shear = 5-10 cm	
Elliptical internal defect	2.93	6.41	16.43	35.36	29.84	61.29
Circular internal defect	1.39	3.09	7.55	16.69	14.79	32.90

Table 4.4. Maximum *J*-value [kN/m], along the crack front at position 3.

Defect	$2a$ = 1 mm Shear = 5-10 cm		$2a$ = 5 mm Shear = 5-10 cm		$2a$ = 10 mm Shear = 5-10 cm		$2a$ = 20 mm Shear = 5-10 cm	
Elliptical internal defect	2.50	4.72	12.92	27.21	24.90	51.51	-	-
Circular internal defect	1.06	2.02	5.77	12.38	11.59	24.54	22.39	46.49

4.2.4 Damage tolerance analysis using fracture toughness data from IP19

In the damage tolerance analysis, with postulated defects, the critical defect size is given using the failure criteria $J = J_{mat}$ and the acceptable defect size is given using the criteria $J = J_{mat} / SF_J$. In these equations, J is the applied J-value as given in Table 4.2-4.4, J_{mat} is the fracture toughness (with or without some stable crack growth) of the nodular cast iron used in the insert. SF_J is the safety factor used when calculating the acceptable defect size.

As shown in section 2.3, the nodular cast iron has predominantly ductile fracture behaviour. This means that the material does not break when J reaches the initiation toughness ($J_{mat} = J_{Ic}$), instead the material experiences stable crack growth. According to a published investigation from SSM [17], it is reasonable to use a toughness value at 2 mm of stable crack growth for a ductile material. This is especially true in this case, since the insert is subjected to a short-term displacement controlled loading (i.e. not in load control and therefore could be considered as a secondary load). Therefore, J_{mat} should be equal to J_{2mm} in this case.

For the choice of safety factor SF_J, the objective has been to retain the safety margins expressed in ASME Sect. XI [13]. This means that SF_J = 10 is used in the case of normal operation or with loads that occur quite frequently. SF_J = 2 is then used for loads with a very low probability of occurrence. According to the design premises for the canister [18], the probability of occurrence is approximately 6.7E-4 (in the case of a 5 cm shear movement during an earthquake). Therefore, SF_J should be equal to 2 in this case.

Below, the results from the damage tolerance analysis are given. In the analysis the following assumptions has been made:

- The fracture toughness value used is $J_{2mm} = 78$ kN/m (given at 0°C).
- Maximum *J*-value, along the crack front is used in the analysis (see Table 4.2-4.4).
- When calculating critical defect sizes, the safety factor SF_J = 1.0.
- When calculating acceptable defect sizes, the safety factor SF_J = 2.0.

Table 4.5. Acceptable and critical defect sizes for postulated defects.

Defect assumption	Position of the defect	Acceptable depth Shear = 5-10 cm		Acceptable length Shear = 5-10 cm	
Semi-elliptical surface defect	1	4.1	1.7	24.6	10.2
Semi-circular surface defect	1	7.5	2.7	15.0	5.4
Elliptical internal defect	2	> 10	5.7	> 60	34.2
Circular internal defect	2	> 10	> 10	> 10	> 10
Elliptical internal defect	3	> 10	7.4	> 60	44.4
Circular internal defect	3	> 20	16.6	> 20	16.6
		Critical depth Shear = 5-10 cm		Critical length Shear = 5-10 cm	
Semi-elliptical surface defect	1	9.7	3.2	58.2	19.2
Semi-circular surface defect	1	> 10	5.5	> 20	11.0
Elliptical internal defect	2	> 10	> 10	> 60	> 60
Circular internal defect	2	> 10	> 10	> 10	> 10
Elliptical internal defect	3	> 10	> 10	> 60	> 60
Circular internal defect	3	> 20	> 20	> 20	> 20

When comparing the old results for the BWR insert [2] and the new results for the PWR insert (using a shear displacement equal to 5 cm) it turns out that the calculated *J*-values are quite similar for surface defects. For the semi-elliptical surface defect the BWR-values are only slightly higher (3% at a = 5 mm). For the internal defects, the BWR-values are dominating, i.e. for the elliptical internal defects the BWR-values are 25% larger (at a = 5 mm). But since the fracture toughness values for PWR inserts is smaller than BWR inserts ($J_{2\text{mm}} = 78$ kN/m compared to $J_{2\text{mm}} = 88$ kN/m), the acceptable defect depth for semi-elliptical surface defect are almost identical (PWR a_{acc} = 4.1 mm and BWR a_{acc} = 4.5 mm).

Only qualified data [9-10], according to ASTM E1820 (Standard Test Method for Measurement of Fracture Toughness), are used to derive the results given in Table 4.5. These qualified fracture toughness data are taken from positions close to the outer surface of the insert, which is relevant for surface defects and internal defects in position 2. For defects in position 3, there are only non-qualified data available (two data points, IP19T-2 and IP19T-5 [9-10]) and therefore fracture toughness data from positions close to the outer surface are used in this position also. However, since the non-qualified data points IP19T-2 and IP19T-5 are also the data with the lowest fracture toughness values (both at initiation and at 2 mm of stable crack growth), a sensitivity analysis is performed. Of all the data points, $J_{2\text{mm}} = 67$ kN/m is the lowest, using the data point IP19T-5 [9-10]. A revised damage tolerance analysis for postulated defects in position 3, using non-qualified fracture toughness data close to this position are therefore given in Table 4.6.

Table 4.6. Acceptable and critical defect sizes for postulated defects in position 3, using non-qualified fracture toughness data close to this position ($J_{2mm} = 67$ kN/m).

Defect assumption	Position of the defect	Acceptable depth Shear = 5-10 cm		Acceptable length Shear = 5-10 cm	
Elliptical internal defect	3	> 10	6.3	> 60	37.8
Circular internal defect	3	> 20	14.1	> 20	14.1
		Critical depth Shear = 5-10 cm		Critical length Shear = 5-10 cm	
Elliptical internal defect	3	> 10	> 10	> 60	> 60
Circular internal defect	3	> 20	> 20	> 20	> 20

A comparison between Table 4.5 and Table 4.6 shows that using the smallest fracture toughness value (J_{2mm} from IP19T-5) has a minor effect on the calculated acceptable defect sizes. The reason for this is related to the testing of this specimen that shows a large difference on the initiation values and not on the vales at 2 mm of stable crack growth. This is shown in Table 4.7, which indicates that using the fracture toughness value at 2 mm of stable crack growth is questionable in this case.

Table 4.7. A comparison between the qualified fracture toughness data and the non-qualified data from specimen IP19T-5.

Fracture toughness at	Mean value with qualified data [kN/m]	Data from IP19T-5 [kN/m]	Difference
Initiation	32	12	-62 %
2 mm stable crack growth	86	67	-22 %

Finally, it could be interesting to check what J_{2mm}-value (at position 3, shear = 5 cm) that is equivalent to an acceptable depth of 10 mm (elliptical internal defect) and an acceptable depth of 20 mm (circular internal defect).

- An elliptical internal defect with an acceptable depth of 10 mm is equivalent to $J_{2mm} = 50$ kN/m.
- An circular internal defect with an acceptable depth of 20 mm is equivalent to $J_{2mm} = 45$ kN/m.

5 CONCLUSIONS

SKB has asked Inspecta Technology AB to perform a damage tolerance analysis of the PWR iron insert both in the case of a pressure load and a shear load. The purpose of the analysis is to use material data for PWR inserts and compare the results with earlier calculations using material data for BWR inserts.

The main conclusions from the damage tolerance analysis are:

- The limit pressure load is higher using PWR insert material data. This shows that the results using BWR stress-strain data are conservative as regards to plastic collapse of the PWR canister. This is also true in the case of circular defects present in the PWR insert.
- In the case of a pressure load, the acceptable defect sizes are not influenced by the assumption regarding fracture toughness values. The results using BWR- or PWR-data are identical, since compressive stresses dominate when an external pressure is applied to the canister.
- In the case of a shear load, the acceptable defect sizes are slightly influenced by using PWR insert fracture toughness data together with the PWR insert stress-strain curve and the difference in geometry between the BWR and PWR canisters. The resulting acceptable defect depth for semi-elliptical surface defects are a_{acc} = 4.1 mm (for a PWR insert) and a_{acc} = 4.5 mm (for a BWR insert).

6 REFERENCES

SKB's (Svensk Kärnbränslehantering AB) publications can be found at www.skb.se/publications. References to SKB's unpublished documents will be submitted upon request to document@skb.se.

[1] RAIKO, H., SANDSTRÖM, R., RYDÉN, H. and JOHANSSON, M., (2010-04), "Design analys report for the canister", SKB Technical Report TR-10-28, Swedish Nuclear Fuel and Waste Management Co.

[2] DILLSTRÖM, P., ALVERLIND, L. and ANDERSSON, M., (Januari 2010), "Framtagning av acceptanskriterier samt skadetålighetsanalyser för segjärnsinsatsen", SKB Rapport R-10-11, Svensk Kärnbränslehantering AB.

[3] HERNELIND, J., (2010-08), "Modelling and analysis of canister and buffer for earthquake induced rock shear and glacial load", SKB Technical Report TR-10-34, Swedish Nuclear Fuel and Waste Management Co.

[4] DILLSTRÖM, P. and BOLINDER, T., (October 2010), "Damage tolerance analysis of canister inserts for spent nuclear fuel in the case of an earthquake induced rock shear load", SKB Technical Report TR-10-29, Swedish Nuclear Fuel and Waste Management Co.

[5] SANDAHL, P., (2010-06-30), "Stukprovning på gjutjärnsinsatser IP17 och IP19", SKBdoc 1247615, version 2.0, Svensk Kärnbränslehantering AB.

[6] WIHED, M., (2010-05-16), "Kompletterande materialprovning av segjärnsinsats IP 19T", SKBdoc 1242454, version 2.0, Svensk Kärnbränslehantering AB.

[7] WIHED, M., (2010-05-17), "Materialprovning av segjärnsinsats IP 19M", SKBdoc 1242455, version 2.0, Svensk Kärnbränslehantering AB.

[8] WIHED, M., (2010-05-18), "Materialprovning av segjärnsinsats IP 19B", SKBdoc 1242456, version 2.0, Svensk Kärnbränslehantering AB.

[9] ÖBERG, M., (2010-06-22), "Brottmekanisk provning av gjutjärn, IP19T", SKBdoc 1248109, version 2.0, Svensk Kärnbränslehantering AB.

[10] ÖBERG, M., (2010-09-17), "Brottmekanisk provning av gjutjärn, IP19T, IP19M och IP19B", SKBdoc 1255011, version 2.0, Svensk Kärnbränslehantering AB.

[11] AYYUB, B. M., and R. H. MCCUEN., (1997), *Probability, Statistics & Reliability for Engineers*, CRC Press LLC, Boca Raton, Florida.

[12] –, (2004), ASME III Div 1, NB-3200 Design By Analysis, ASME International.

[13] –, (2008), ASME Boiler and Pressure Vessel Code, Sect XI – "Rules for Inservice Inspetion of Nuclear Power Plant Components", ASME International.

[14] –, (2007), ANSYS 11.0, Swanson Analysis Systems Inc, 2007.

[15] DILLSTRÖM, P., and W. ZANG., (2004), "User manual ProSACC Version 1.0", DNV Research Report 2004/02, Det Norske Veritas AB, Stockholm, Sweden.

[16] –, (2009), ABAQUS Manuals, Dassault Systèmes Simula Corp.

[17] BRICKSTAD, B., (2009-03-17), "Analys av driftinducerade skador i svenska kärntekniska anläggningar", Utredningsrapport SSM 2008/232, Swedish Radiation Safety Authority.

[18] —, (Nov. 2009), "Design premises for a KBS-3V repository based on results from the safety assessment SR-Can and some subsequent analyses", Technical Report TR-09-22, Swedish Nuclear Fuel and Waste Management Co.

7 TABLE OF REVISIONS

Rev.	Activity / Purpose of this revision	Handled by	Date
0	—	Peter Dillström	2011-02-22
1	New postulated defect in position 3. Sensitivity analysis for defects in position 3.	Peter Dillström	2011-07-06
2	Introduced a clarification regarding the purpose of this report (in the introduction).	Peter Dillström	2012-05-15
3	Revised according to comments made by SKB.	Peter Dillström	2013-10-01
4	Revised according to comments made by SKB (DocID 1401552).	Peter Dillström	2013-12-22
5	Figure 2.4 is removed from Section 2.3.	Peter Dillström	2014-01-08
6	Introduced changes in the report to emphasize that the material testing of IP17 and IP19 was performed in 2010.	Peter Dillström	2014-01-12
7	Revised according to comments made by SKB (DocID 1421055, Ver. 0.2).	Peter Dillström	2014-01-23
8	Revised according to comments made by SKB (DocID 1421055, Ver. 0.4).	Peter Dillström	2014-01-31

8 APPENDIX A. CALCULATED *J*-VALUES WHEN USING A BENTONITE DENSITY OF 2050 KG/M^3

The results below (for the model *model6g_PWR2_normal_quarter_2050ca3*) are presented in graphs, using one graph for each type of defect and crack depth. In each graph results along the crack front from two different load magnitudes are plotted (the angle ϕ is defined in Fig. 4.6). Each load magnitude corresponds to 5 and 10 cm shear of the PWR canister including the bentonite clay.

8.1 *J*-values for a semi-elliptical surface defect at position 1, using a bentonite density of 2050 kg/m^3

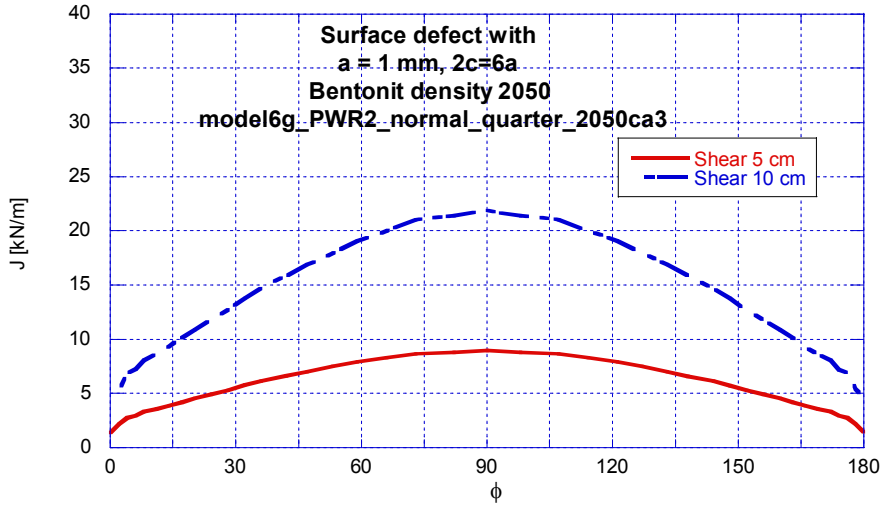

Figure 8.1. *J*-integral for a semi-elliptical surface defect plotted along the crack front (a = 1 mm).

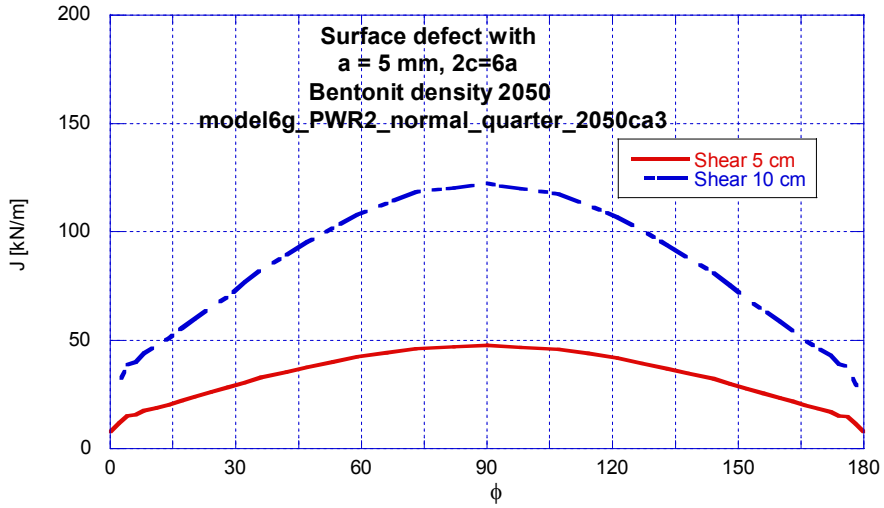

Figure 8.2. *J*-integral for a semi-elliptical surface defect plotted along the crack front (a = 5 mm).

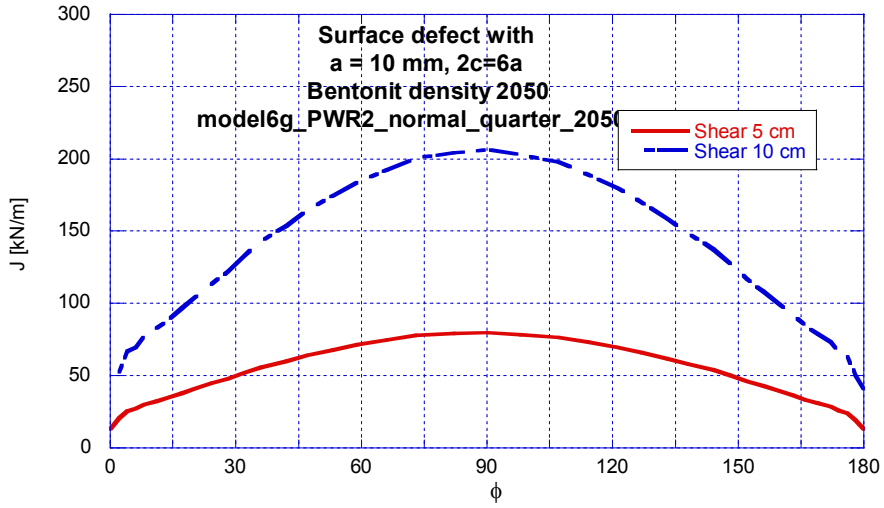

Figure 8.3. *J*-integral for a semi-elliptical surface defect plotted along the crack front (a = 10 mm).

8.2 *J*-values for a semi-circular surface defect at position 1, using a bentonite density of 2050 kg/m^3

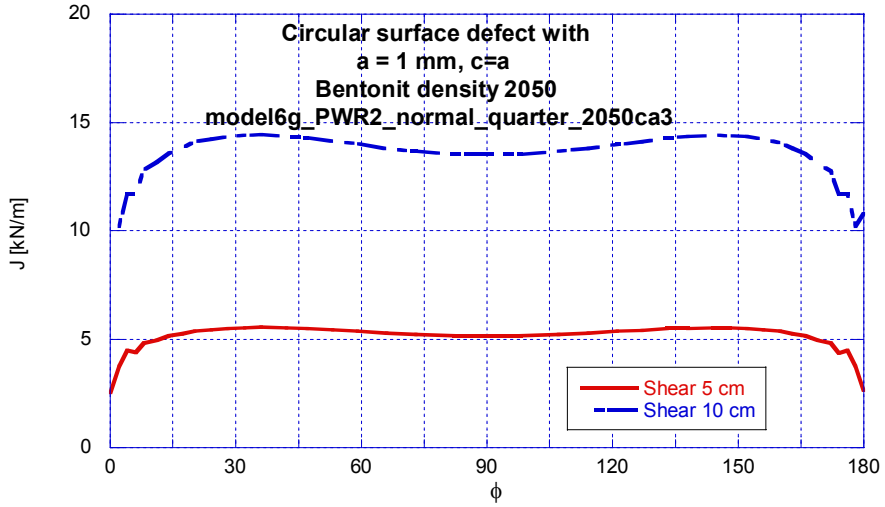

Figure 8.4. *J*-integral for a semi-circular surface defect plotted along the crack front (a = 1 mm).

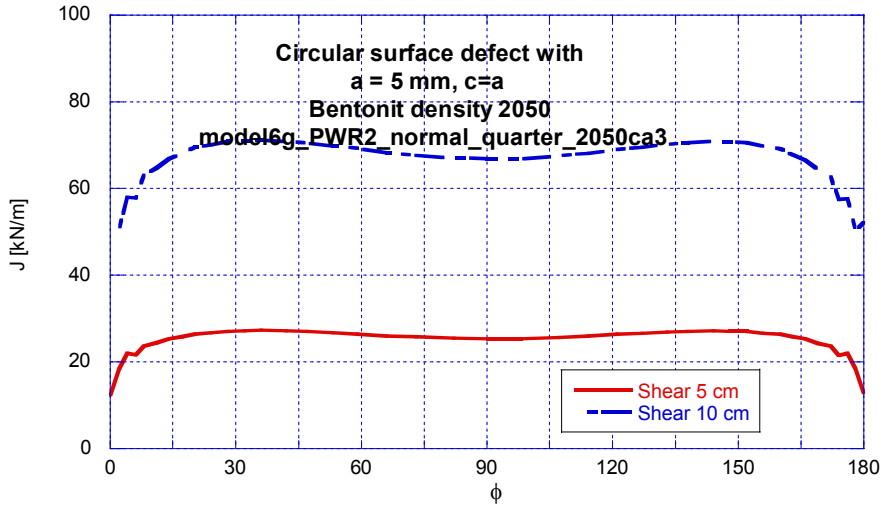

Figure 8.5. *J*-integral for a semi-circular surface defect plotted along the crack front (a = 5 mm).

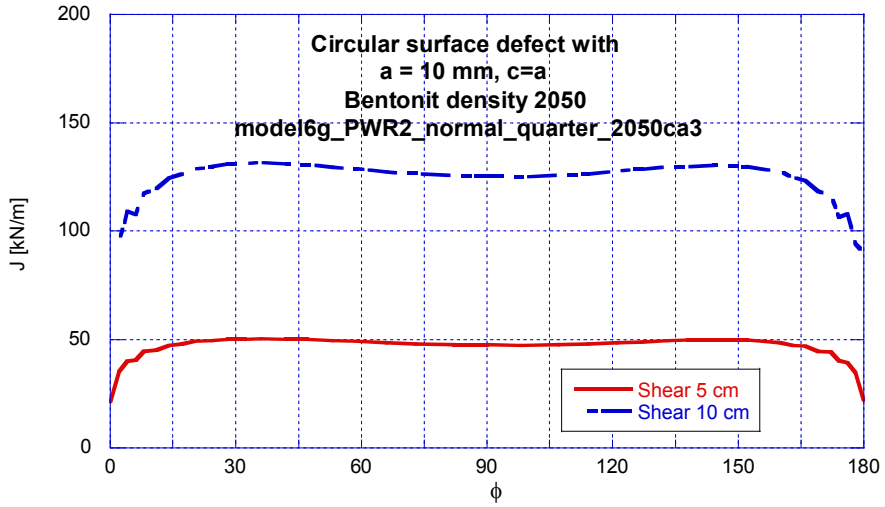

Figure 8.6. *J*-integral for a semi-circular surface defect plotted along the crack front (a = 10 mm).

8.3 *J*-values for an internal elliptical defect at position 2, using a bentonite density of 2050 kg/m^3

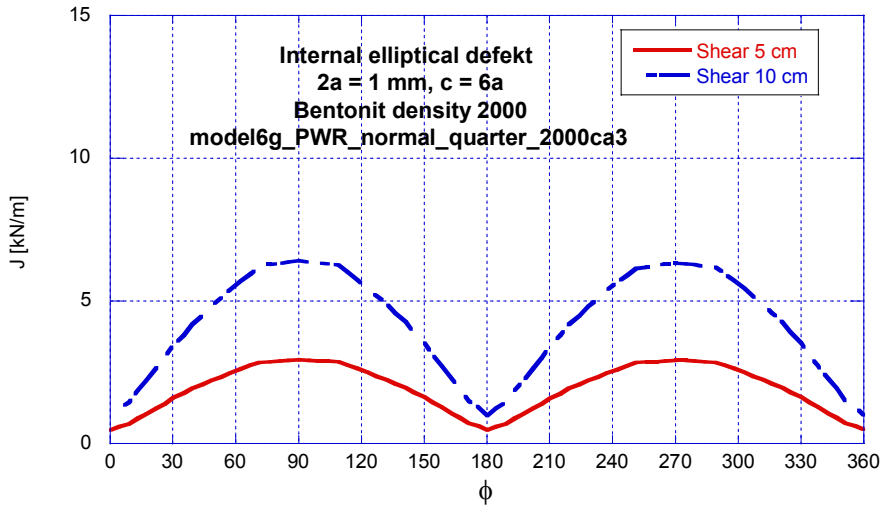

Figure 8.7. *J*-integral for an internal elliptical defect plotted along the crack front ($2a$ = 1 mm).

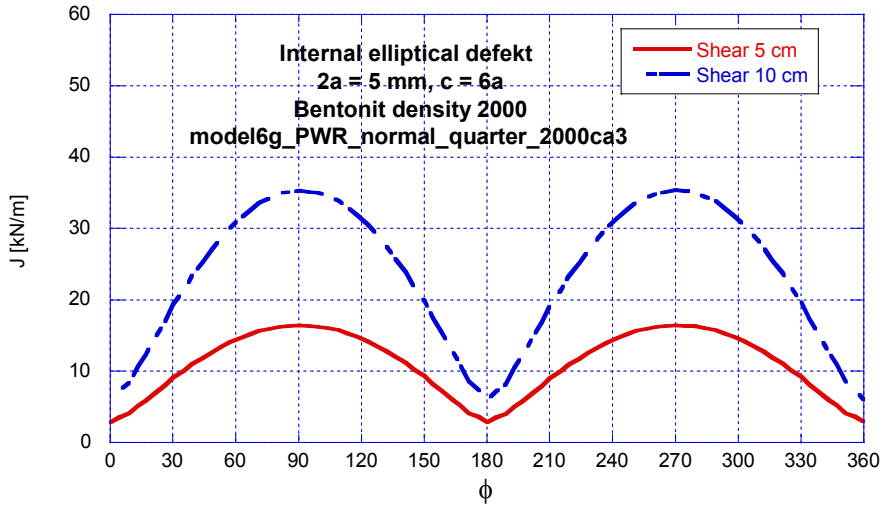

Figure 8.8. *J*-integral for an internal elliptical defect plotted along the crack front ($2a$ = 5 mm).

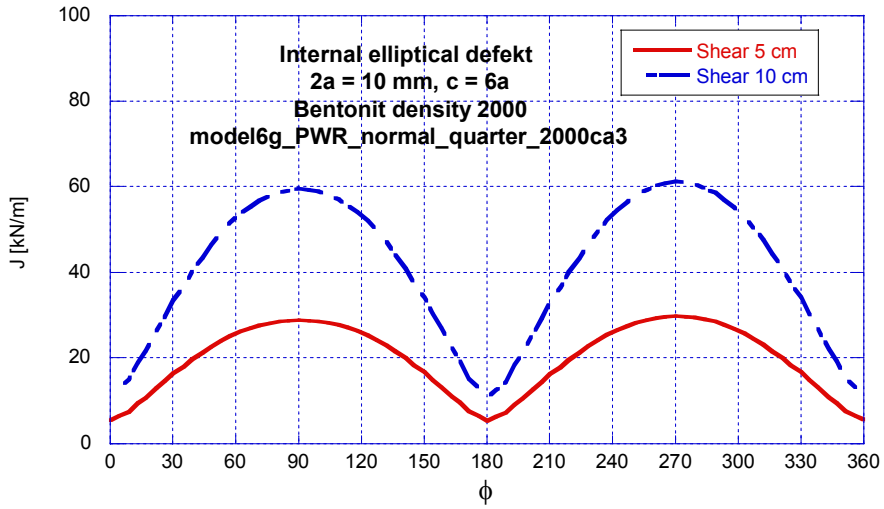

Figure 8.9. *J*-integral for an internal elliptical defect plotted along the crack front ($2a$ = 10 mm).

8.4 *J*-values for an internal circular defect at position 2, using a bentonite density of 2050 kg/m^3

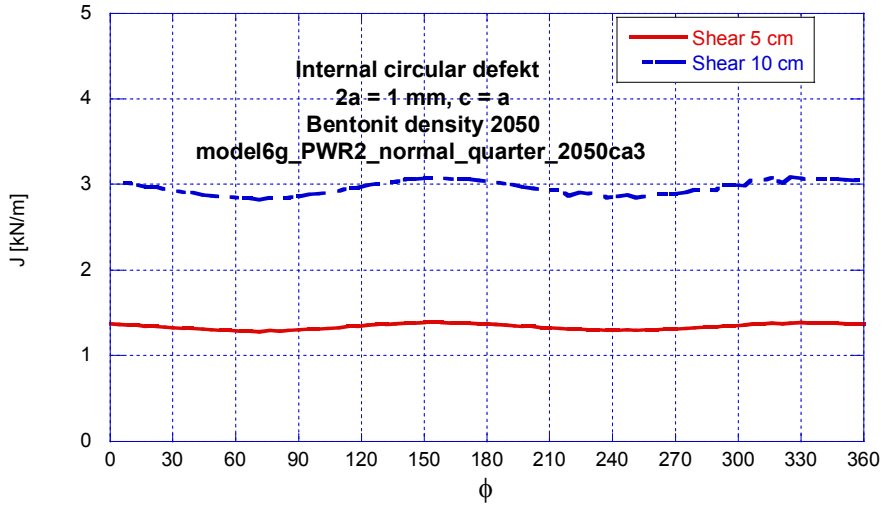

Figure 8.10. *J*-integral for an internal circular defect plotted along the crack front ($2a$ = 1 mm).

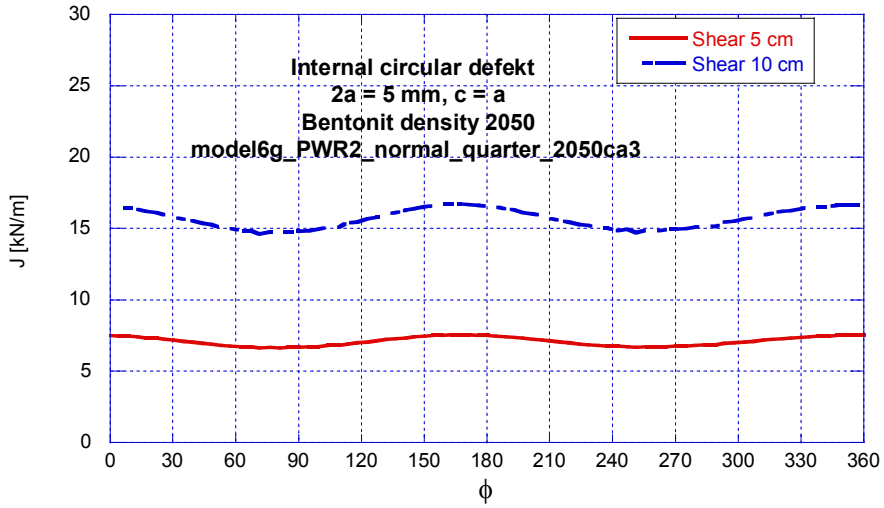

Figure 8.11. *J*-integral for an internal circular defect plotted along the crack front ($2a$ = 5 mm).

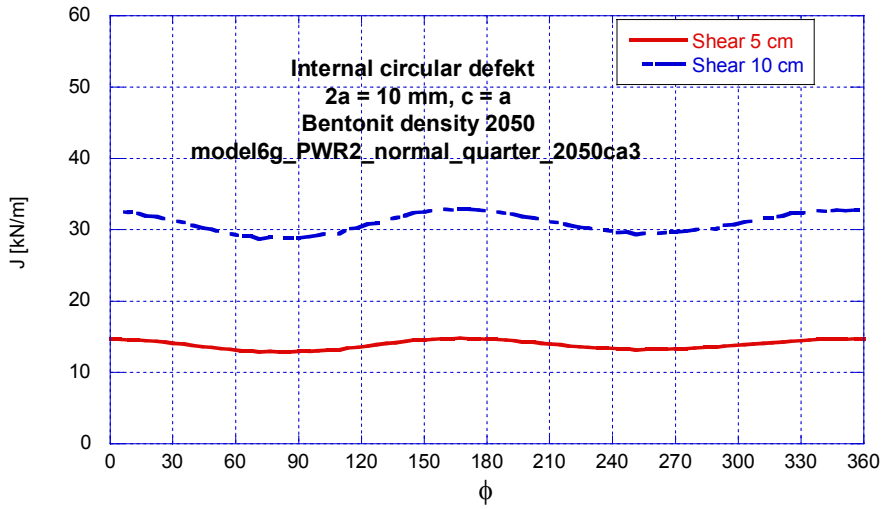

Figure 8.12. *J*-integral for an internal circular defect plotted along the crack front ($2a$ = 10 mm).

8.5 *J*-values for an internal elliptical defect at position 3, using a bentonite density of 2050 kg/m^3

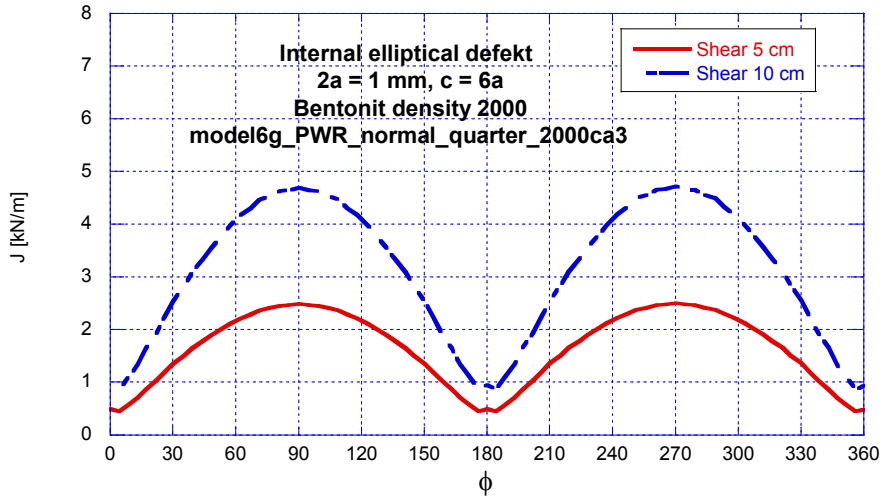

Figure 8.13. *J*-integral for an internal elliptical defect plotted along the crack front ($2a$ = 1 mm).

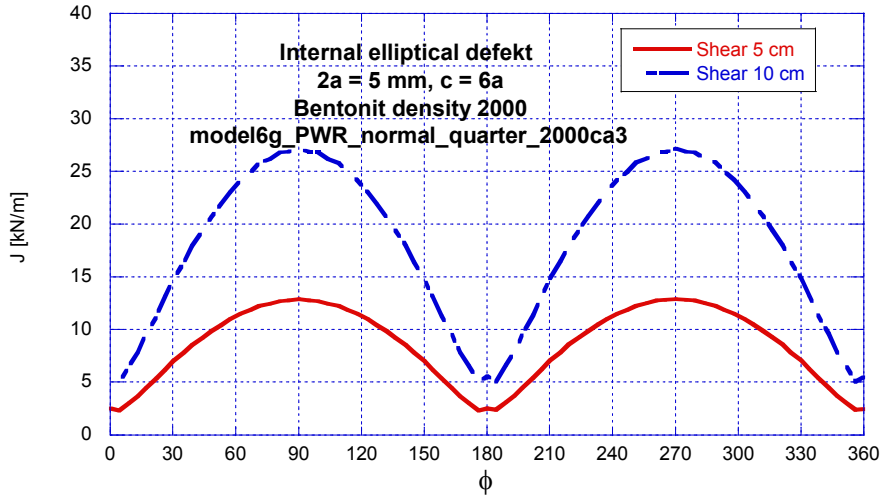

Figure 8.14. *J*-integral for an internal elliptical defect plotted along the crack front ($2a$ = 5 mm).

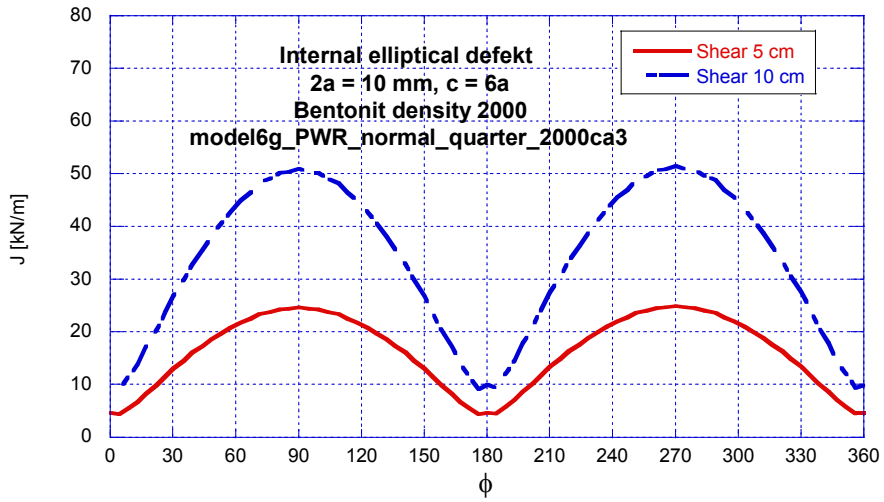

Figure 8.15. *J*-integral for an internal elliptical defect plotted along the crack front ($2a$ = 10 mm).

8.6 *J*-values for an internal circular defect at position 3, using a bentonite density of 2050 kg/m^3

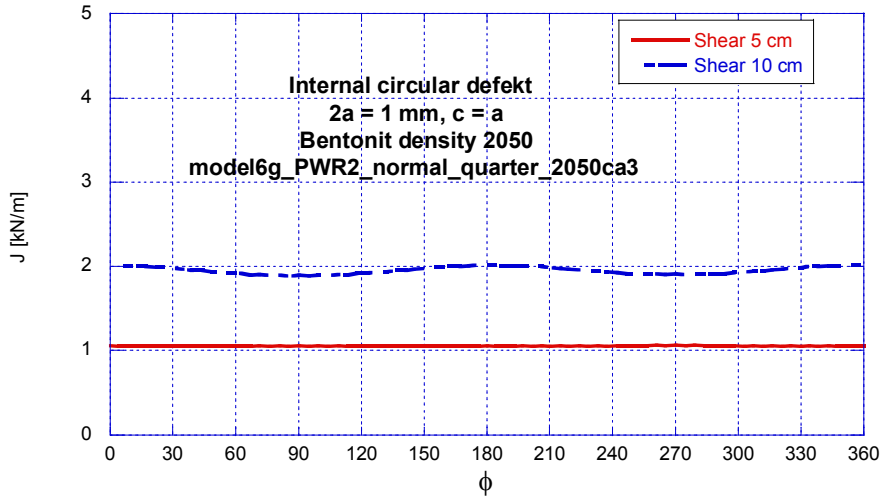

Figure 8.16. *J*-integral for an internal circular defect plotted along the crack front ($2a$ = 1 mm).

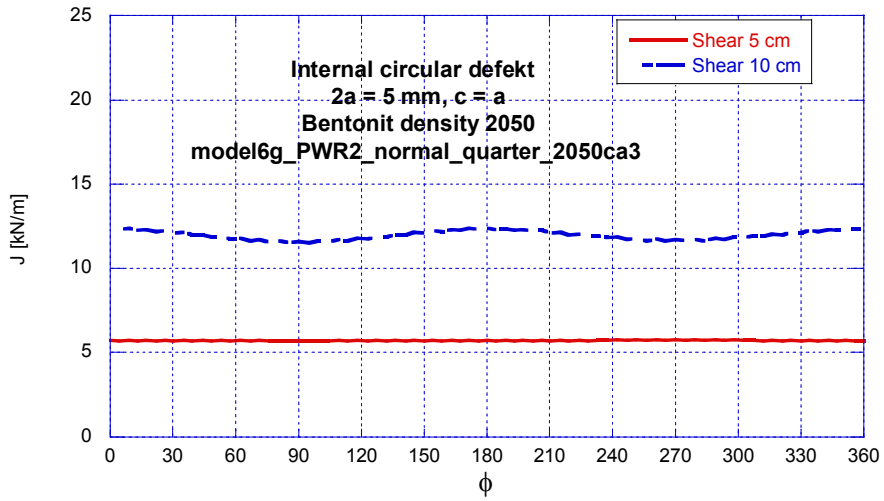

Figure 8.17. *J*-integral for an internal circular defect plotted along the crack front ($2a$ = 5 mm).

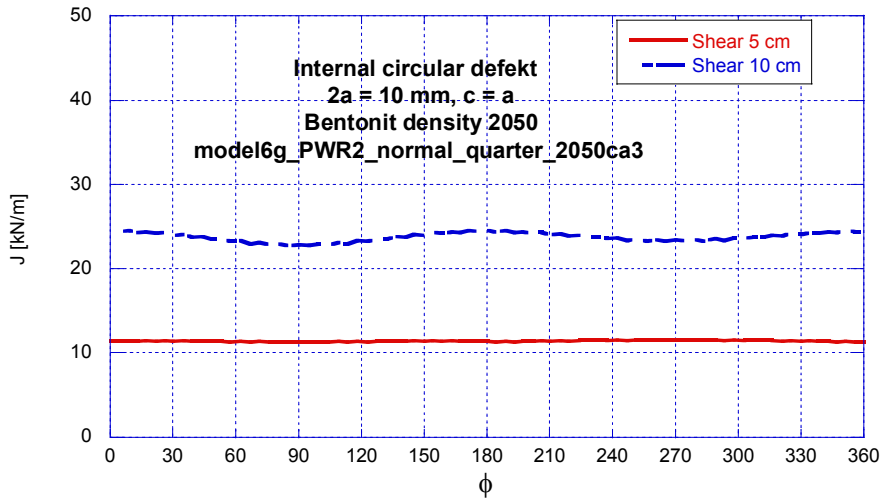

Figure 8.18. *J*-integral for an internal circular defect plotted along the crack front ($2a$ = 10 mm).

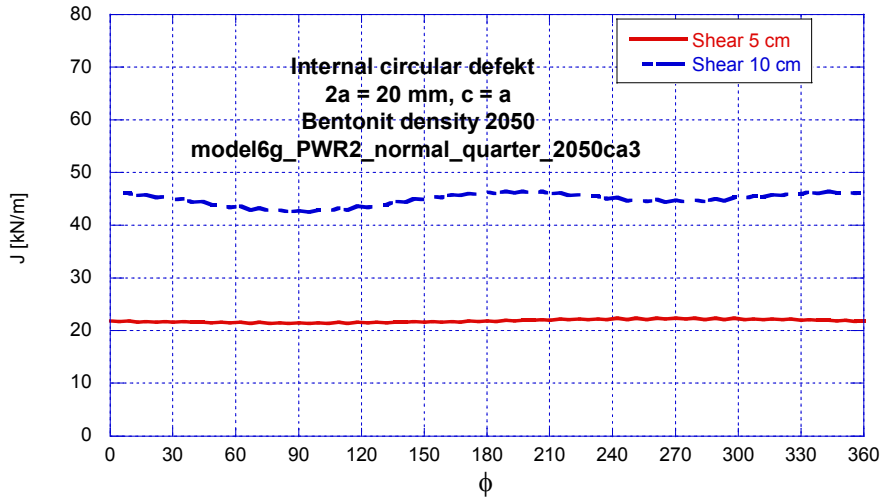

Figure 8.19. *J*-integral for an internal circular defect plotted along the crack front ($2a$ = 20 mm).